Physics – Uspekhi **67** (9) 855 – 865 (2024)

REVIEWS OF TOPICAL PROBLEMS

PACS numbers: **03.67. – a**, 42.50.Dv, 85.25.Cp

ON THE 90TH ANNIVERSARY OF THE P.N. LEBEDEV PHYSICAL INSTITUTE (LPI)

Quantum memristors: a new approach to neuromorphic computing

P A Forsh, S Yu Stremoukhov, A S Frolova, K Yu Khabarova, N N Kolachevsky

DOI: https://doi.org/10.3367/UFNe.2024.06.039698

Contents

Abstract. We present a review on quantum memristors, which define a new direction for neuromorphic applications. We discuss the general methodology and concept of constructing a quantum memristor, as well as the possibility of its implementation on photonic platforms, superconducting systems, and ultracold trapped ions. The latter platform is being actively developed at the Lebedev Physical Institute for conducting quantum computations and for building a high-performance quantum computer; it has also proven its worth in creating optical clocks.

Keywords: memristors, quantum computing, neuromorphic systems

1. Introduction

The term 'memristor' (resistor with memory) was coined in the early 1970s by Chua [1], who hypothesized the existence of a memristor as a fourth fundamental element of a passive circuit, along with a resistor, capacitor, and inductor. Chua's work remained largely unnoticed until 2008, when Strukov and colleagues [2] reported an experimental implementation of a memristor. A memristor is a nonvolatile, bipolar memory device whose resistance depends on the charge that has passed through it. After the voltage in the circuit is disconnected, the memristor 'remembers' the last resistance value and thus retains the memory of previous states. We note that later studies challenged Chua's conceptual direction, questioning the status of the memristor as a fundamental fourth element (see, e.g., [3, 4]), and the memristor implemented by Strukov was radically different from what Chua had in mind. However, historically, the name memristor has stuck for a 'resistor with memory.'

It was soon realized that memristors carry the potential to revolutionize electronics by allowing information to be stored without a power source [5] and also imitate the behavior of neural synapses [6, 7]. The ability of a memristor to combine data storage and computation in a single element is ideal for hardware implementations of bio-inspired neural networks. This opens up a wide range of applications for memristors in physical neural networks and neuromorphic architectures. In addition, the memory formalism is applicable to a wide range of physical and biological systems, which allows its application to extend far beyond electronics.

In Strukov's work, the memristor was a thin layer of TiO_2 placed between two electrodes. Under the effect of a high voltage applied to the electrodes, the migration of oxygen vacancies within TiO_2 occurred, which reduced the resistance of the system, because oxygen vacancies in titanium oxide are donor impurities. The studied structure and the process of migration of oxygen vacancies are schematically shown in Fig. 1.

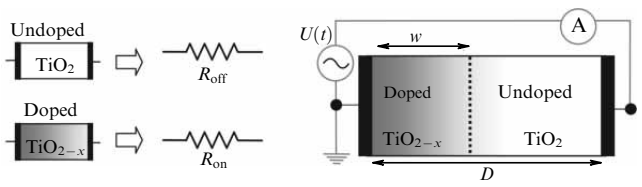

Figure 1. Structure of a memristor [2].

P A Forsh [1, 2, a], **S Yu Stremoukhov** [1, 2, 3, b], **A S Frolova** [1, 2], **K Yu Khabarova** [2, c], **N N Kolachevsky** [2, 4, d]
[1] Lomonosov Moscow State University, Leninskie gory 1, 119991 Moscow, Russian Federation
[2] Lebedev Physical Institute, Russian Academy of Sciences, Leninskii prosp. 53, 119991 Moscow, Russian Federation
[3] National Research Center Kurchatov Institute, pl. Akademika Kurchatova 1, 123182 Moscow, Russian Federation
[4] Russian Quantum Center, Bol'shoi bul'var 30, str. 1, 121205 Skolkovo, Moscow, Russian Federation
E-mail: [a] forshpa@lebedev.ru, [b] sustrem@gmail.com, [c] kseniakhabarova@gmail.com, [d] kolachevsky@lebedev.ru

Received 21 May 2024, revised 19 June 2024
Uspekhi Fizicheskikh Nauk **194** (9) 905 – 916 (2024)
Translated by S Alekseev

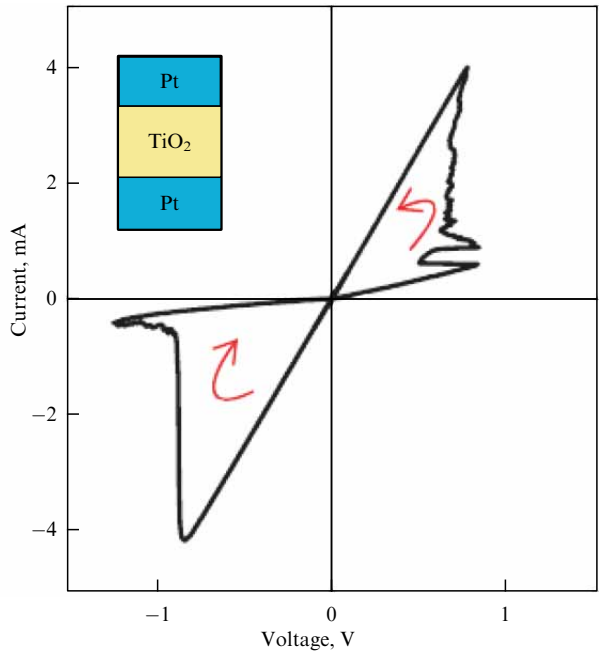

Figure 2. Experimentally observed current–voltage characteristic of the $Pt-TiO_{2-x}-Pt$ structure [2].

The current–voltage characteristic of the memristor is determined by the equations

$$U(t) = \left(R_{on}\frac{w(t)}{D} + R_{off}\left(1 - \frac{w(t)}{D}\right)\right) I(t)\,, \tag{1}$$

$$\frac{dw(t)}{dt} = \mu\frac{R_{on}}{D}\,I(t)\,, \tag{2}$$

where $U(t)$ and $I(t)$ are the voltage and current in the structure, R_{off} and R_{on} are the resistances of titanium oxide in the nonconducting (without oxygen vacancies) and conducting (with oxygen vacancies) states, D is the film thickness, $w(t)$ is the thickness of the titanium oxide region with oxygen vacancies at a time t, and μ is the oxygen ion mobility. Under the condition $R_{on} \ll R_{off}$, it follows from Eqns (1) and (2) that the memristor resistance is

$$R(q) = R_{off}\left(1 - \frac{\mu R_{on}}{D^2}\,q(t)\right), \tag{3}$$

where $q(t)$ is the charge flowing through the structure. In formula (3), the dependence of the resistance on the charge flowing through it is the main feature that distinguishes a memristor and gives rise to a hysteresis curve that passes through the origin on its current–voltage characteristic (Fig. 2).

At present, a large number of memristors are being created based on various inorganic (TiO_2, ZnO, HfO_2, WO_3, SiO_2, and many others) [8–13] and organic [14–19] materials. Along with memristors, memcapacitors and meminductors have also attracted interest [20, 21]. Each of them, like the memristor, is characterized by a certain dependence of its characteristic (capacitance or inductance) on the initial state and the effects applied to the system starting with the initial time instant. Memristive devices (memelements) have a wide range of applications in physical neural networks and neuromorphic architectures [22–29]. Moreover, the formalism of memory devices is applicable to a wide range of physical and biological systems and allows extending these concepts far beyond the field of electronics [30].

In its most general formulation, a memelement is defined by some input parameter x and an output parameter y (for example, in the case of a current-controlled memristor, these are the current and voltage) and the so-called state parameter $s(t)$, which changes in time in accordance with a certain law [31]. These parameters are related as

$$y = f(s, x, t)x\,, \tag{4}$$

$$\frac{ds}{dt} = g(s, x, t)\,, \tag{5}$$

where $f > 0$ and g are functions that determine the dynamics of the system. The state parameter $s(t)$ carries information about the physical state of the system [32] and tracks the past configuration of the memristor using the update function g [33]. Evidently, formulas (1) and (2) are a special case of formulas (4) and (5).

Almost all memristive devices created and studied to date have classical input and output signals (x and y). A natural question arises as to whether a memristive device is possible that would demonstrate a hysteresis curve in the input–output characteristic and at the same time exhibit a truly quantum behavior, which would then allow processing quantum information. In accordance with the current trend, such a device is called a quantum memristor (although it should better be called a quantum memelement); its concept was outlined by Pfeiffer et al. in [34]. A quantum memristor is a device that exhibits quantum coherence together with 'memristive behavior' in the classical limit. Thus, a quantum memristor combines the advantages of quantum computing with the ability to store information, which distinguishes it favorably from both quantum information storage devices [35] and quantum computing devices [36]. Quantum advantages include much faster computation due to quantum parallelism and genuine quantum properties such as entanglement, while the memory behavior is a nonlinear feature that goes beyond a purely unitary evolution (which is necessarily linear) and allows implementing quantum neuromorphic computations. Due to the inherent linearity of quantum mechanics, it is challenging to describe a dissipative nonlinear memory element such as a memristor in the quantum domain, because nonlinearities typically lead to the violation of fundamental quantum principles. Indeed, the 'memristive nature' requires non-Markovian behavior that cannot be realized by simply performing unitary operations on a closed quantum system. Thus, a quantum memristor requires an open quantum system coupled to a dissipative environment, with the coupling between the system and the environment established via a weak measurement scheme and classical feedback. The coupling to the environment must be strong enough to ensure 'memristive behavior,' but weak enough to preserve the required level of quantum coherence.

At present, the development of quantum memristors and their use in neuromorphic computing is still in the early stages. There are several well-developed proposals for the implementation of a quantum memristor in superconducting circuits using memory effects that naturally occur in Josephson junctions. Also, a rather effective approach to creating a quantum memristor currently appears to be provided by quantum photonic platforms and trapped ultracold ions.

The concept of a quantum memristor based on trapped ultracold ions was first proposed by researchers from the Lebedev Physical Institute as a natural continuation of the many years of research in the field of ion frequency standards and quantum computing based on this platform [37–39]. In this review, we provide basic information on the implementation of quantum memristors on these platforms.

2. Quantum memristors on photonic platforms

The key element of a quantum memristor based on quantum photonics is a beam splitter whose reflectivity can be adjusted depending on the measurement results in one of the outgoing beams [32]. This feedback mechanism provides memory and nonlinear behavior, while photonic degrees of freedom implement quantum coherence. A similar implementation of a quantum memristor can be achieved using frequency-entangled optical fields and a frequency mixer that, similarly to a beam splitter, creates superpositions of states [40].

In [32], a quantum memristor is presented, the fundamental components of which — a tunable dissipative element, a detector, and a classical response — are assembled on a quantum photonics platform. The experimental implementation of the dissipative element is a Mach–Zehnder interferometer with two semitransparent mirrors, a wave plate that introduces a phase shift θ between the channels, and two compensating wave plates (Fig. 3). This design is equivalent to a beam splitter with an arbitrary reflectivity. The beam splitter plays the role of a tunable device for communicating with the environment.

Following [32], we consider the formation of the beam splitter output signal using coherent states as an example. We assume an initial coherent state $|\alpha\rangle$ in beam a_1 and a vacuum state in beam a_2; then, the final states in respective beams b_1 and b_2 are $|\alpha\cos(\theta/2)\rangle_{b_1}$ and $|\alpha\sin(\theta/2)\rangle_{b_2}$. We choose the mean value of the amplitude of the input beam a_1 as an

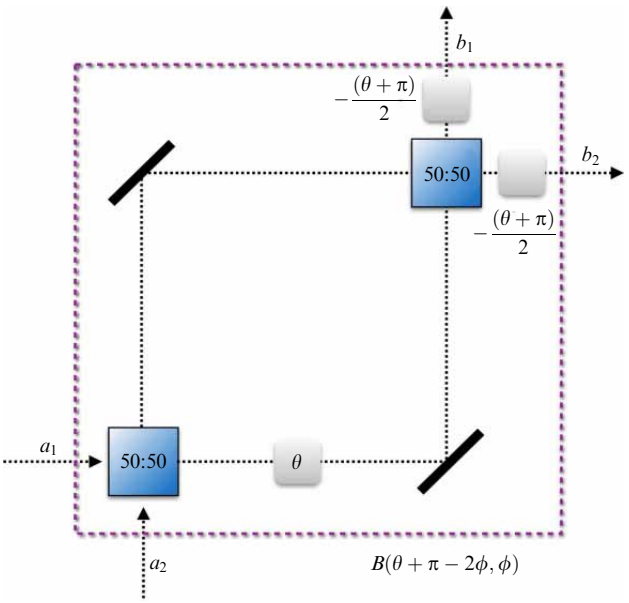

Figure 3. Two semi-transparent mirrors and three wave plates in Mach–Zehnder scheme form an effective beam splitter with an arbitrary reflectivity. Because the phase shift of the wave plate can be directly controlled, the device is suitable for building a quantum memristor on a quantum photonics platform [32].

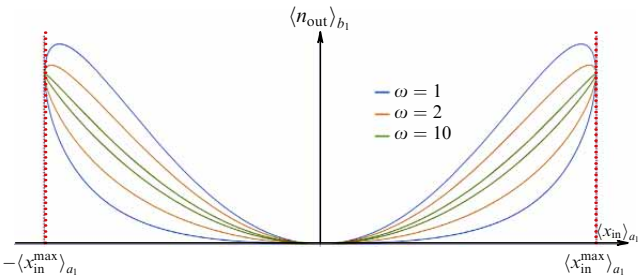

Figure 4. Hysteresis loops for coherent states in variables $\langle n_{\text{out}}\rangle_{b_1}$ and $\langle x_{\text{in}}\rangle_{a_1}$. Dependences are shown for three different frequencies of the periodic signal [32].

independent variable:

$$\langle x_{\text{in}}\rangle_{a_1} = \text{Re}\,(\alpha)\,.$$

The memristor is a dissipative element, and therefore the number of photons in beam b_1 changes, which allows this quantity to be regarded as a dependent variable. We choose the output signal to be

$$\langle n_{\text{out}}\rangle_{b_2} = |\alpha|^2 \sin^2\frac{\theta}{2}\,.$$

The output state can be controlled by changing the reflectivity of the beam splitter using the phase θ.

On the other hand,

$$\langle n_{\text{out}}\rangle_{b_1} = |\alpha|^2 \cos^2\frac{\theta}{2}\,.$$

This allows writing the relation between the input and output signals as

$$\langle n_{\text{out}}\rangle_{b_1} = f\left(\theta, \langle x_{\text{in}}\rangle_{a_1}\right)\langle x_{\text{in}}\rangle_{a_1}\,. \tag{6}$$

We have

$$\dot{\theta} = g\left(\theta, \langle x_{\text{in}}\rangle_{a_1}\right). \tag{7}$$

Equations (6) and (7) define the memristive behavior of the system. In the case where

$$\langle x_{\text{in}}\rangle_{a_1} = \langle x_{\text{in}}^{\max}\rangle_{a_1}\cos(\omega t)\,,$$

with $\langle x_{\text{in}}^{\max}\rangle_{a_1} = \alpha$, the function

$$f\left(\theta, \langle x_{\text{in}}\rangle_{a_1}\right) = \langle x_{\text{in}}\rangle_{a_1}\cos^2\frac{\theta}{2}$$

can be interpreted as the transmitted intensity per unit of initial displacement. The function $g(\theta, \langle x_{\text{in}}\rangle_{a_1})$ that defines the beam splitter reflectivity can be chosen arbitrarily. In [32], $\dot{\theta}$ was chosen to be directly proportional to $\langle x_{\text{in}}\rangle_{a_1}$. The dependences of $\langle n_{\text{out}}\rangle_{b_1}$ on $\langle x_{\text{in}}\rangle_{a_1}$ are shown in Fig. 4. As was expected, we can see a closed hysteresis loop, which indicates that this system behaves like a memristor with respect to these variables.

This dynamics is closely related to refractive optical bistability, where an optical mechanism is used to change the refractive index in inverse proportion to the light source intensity. Optical bistability is the property of optical devices to exhibit two resonant states, either stable or dependent on the input state. In other words, for a given input signal intensity, two different output signal intensities are possible,

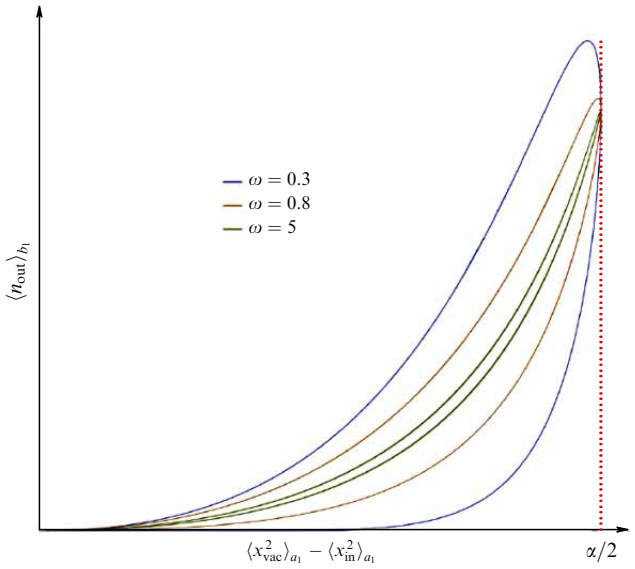

Figure 5. Hysteresis loops for squeezed states of light in variables $\langle n_{\text{out}}\rangle_{b_1}$ and $\langle x^2_{\text{vac}}\rangle_{a_1} - \langle x^2_{\text{in}}\rangle_{a_1}$. Dependences are shown for three different frequencies of the periodic signal [32].

and we need to know the previous states to determine which is the correct, non-Markovian one. This property is attended by a hysteresis loop in the output intensity plotted versus the periodic input intensity.

The system under consideration also exhibits memristive behavior if one input channel of the beam splitter remains in the vacuum state and the other channel is in a squeezed light state $\zeta = r\exp(\mathrm{i}\varphi)$. Then [32],

$$\langle n_{\text{out}}\rangle_{b_1} = \sinh^2 r\cos^2\frac{\theta}{2}\,, \quad \langle n_{\text{out}}\rangle_{b_2} = \sinh^2 r\sin^2\frac{\theta}{2}\,.$$

We can choose the independent variable as the variance

$$\langle x^2_{\text{in}}\rangle_{a_1} = \frac{1}{2}\left(1 + \sinh^2 r - \sinh(2r)\cos\varphi\right),$$

which characterizes the squeezed state. For the vacuum state,

$$\langle x^2_{\text{vac}}\rangle_{a_1} = \frac{1}{2}\,.$$

In this case (assuming that θ depends on $\sin(\omega t)$ linearly), hysteresis is observed in the dependence of $\langle n_{\text{out}}\rangle_{b_1}$ on $\langle x^2_{\text{vac}}\rangle_{a_1} - \langle x^2_{\text{in}}\rangle_{a_1}$. In Fig. 5, these dependences are shown for different values of ω.

Of great interest for encoding quantum *information* are Fock states. We consider a qubit state encoded in the superposition

$$|\Psi\rangle = \exp(\mathrm{i}\alpha)\cos\varphi\,|0\rangle + \sin\varphi\,|1\rangle\,.$$

We feed this state to channel 1, and assume channel 2 to be in the vacuum state. The action of the beam splitter on these states is described by the operator [41]

$$B(\theta,\varphi)|00\rangle = |00\rangle\,,$$

$$B(\theta,\varphi)|10\rangle = \cos\frac{\theta}{2}\,|10\rangle - \exp(\mathrm{i}\varphi)\sin\frac{\theta}{2}\,|01\rangle\,.$$

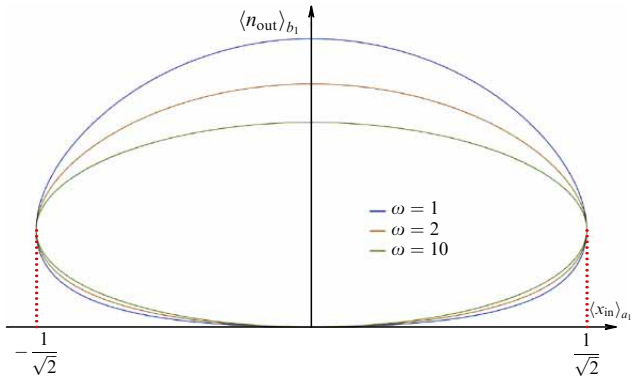

Figure 6. Hysteresis loops for Fock states in variables $\langle n_{\text{out}}\rangle_{b_1}$ and $\langle x_{\text{in}}\rangle_{a_1}$. Dependences are shown for three different frequencies of the periodic signal [32].

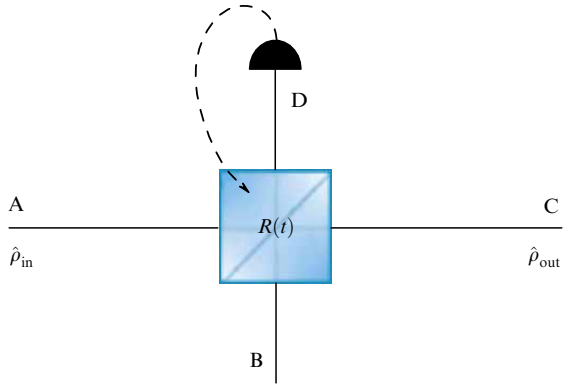

Figure 7. Tunable beam splitter with active feedback. Channel A is used as the input port, and channels C and D as output ports. Reflectivity $R(t)$ is updated based on measurements in channel D [42].

Therefore, the effect of the beam splitter on the superposition is

$$B(\theta,\varphi)|\Psi 0\rangle = \exp(\mathrm{i}\alpha)\cos\varphi\,|00\rangle + \sin\varphi\left(\cos\frac{\theta}{2}\,|10\rangle - \exp(\mathrm{i}\varphi)\sin\frac{\theta}{2}\,|01\rangle\right).$$

We note that the mean value in the $|\Psi\rangle$ state is

$$\langle x_{\text{in}}\rangle_{a_1} = \frac{1}{\sqrt{2}}\sin(2\varphi)\,,$$

and the intensity of light coming out of channel 1 is given by

$$\langle n_{\text{out}}\rangle_{b_1} = \sin^2\varphi\sin^2\frac{\theta}{2}\,.$$

By choosing $\dot{\theta}$ in (7) to be proportional to $\sin(2\omega t)$, we obtain hysteresis in the dependence of $\langle n_{\text{out}}\rangle_{b_1}$ on $\langle x_{\text{in}}\rangle_{a_1}$ (Fig. 6). Here, in contrast to the previous cases, the hysteresis loop does not pass through the origin, which means that the memristor is not passive. This is reflected in the hysteresis area tending to a constant $A \sim \pi/(4\sqrt{2}) + \pi\omega_0/(8\sqrt{2}\omega)$ at high frequencies. Such stability can be useful for quantum information processing.

Fock states and a beam splitter were also used to create a quantum memristor in [42]. The setup is shown in Fig. 7. The

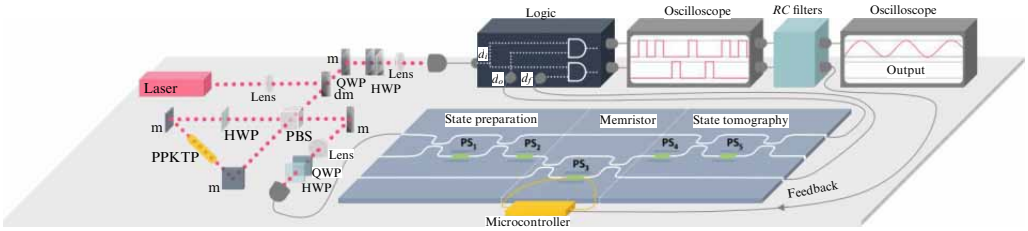

Figure 8. Experimental setup of photonic quantum memristor. When pumped by a continuous wave laser, a spontaneous parametric downconversion source with a periodically polarized KTP (PPKTP) crystal generates orthogonally polarized photon pairs with a wavelength of 1550 nm. Photon pairs are separated by a polarizing beam splitter (PBS), such that measurement of one photon signals the presence of the other, which is injected into the photonic quantum memristor. A state preparation stage consisting of a Mach–Zehnder interferometer with two tunable phase switches (PS) allows creating input state for the quantum memristor. In the final part of the device, photon undergoes a tomography stage, which is used to determine characteristics. A logic block analyzes coincidences among idler photon, output photons, and feedback photons, triggering emission of a rectangular pulse whenever a coincidence is detected. *RC* filters are used to measure photon count for both output and feedback signals [42]. m is a mirror, dm is a beam splitter, QWP is a quarter-wave plate, and HWP is a half-wave plate.

reflectivity $R(t)$ in the beam splitter is tuned and dynamically controlled by active feedback based on the detection of single photons in the output channel D.

The input state (in channel A) is the quantum superposition

$$|\Psi_{\text{in}}\rangle = \alpha(t)\,|0\rangle_{\text{A}} + \beta(t)\,|1\rangle_{\text{A}}\,,$$

where $|\alpha(t)|^2 + |\beta(t)|^2 = 1$, and $|0\rangle_{\text{A}}$ and $|1\rangle_{\text{A}}$ are the vacuum and one-photon states in channel A. Thus, channel A can either contain one photon with the probability $|\beta(t)|^2$ or contain no photons with the probability $|\alpha(t)|^2$. If a photon is detected by detector D after reflection, then the output of channel C is simply the vacuum state $|0\rangle$. But if detector D does not register a photon, then the output state in channel C is

$$\big|\Psi_{\text{out,C}}(t)\big\rangle = \frac{\alpha(t)}{\sqrt{N}}\,|0\rangle_{\text{C}} + \frac{\beta(t)}{\sqrt{N}}\sqrt{1-R(t)}\,|1\rangle_{\text{C}}\,,$$

where N is the normalization constant. This state is still a quantum superposition. To prove this, the authors of [42] define the state after reflection in channels D and C by the wave function

$$\begin{aligned}\big|\Psi_{\text{out,CD}}(t)\big\rangle &= \alpha(t)|0\rangle_{\text{C}}\,|0\rangle_{\text{D}} + \beta(t)\sqrt{1-R(t)}\,|1\rangle_{\text{C}}\,|0\rangle_{\text{D}} \\ &\quad + \mathrm{i}\beta(t)\sqrt{R(t)}\,|0\rangle_{\text{C}}\,|1\rangle_{\text{D}}\,.\end{aligned}$$

The density operator corresponding to this state is

$$\begin{aligned}\rho_{\text{out,CD}} &= \big|\Psi_{\text{out,CD}}(t)\big\rangle\big\langle\Psi_{\text{out,CD}}(t)\big| \\ &= |\alpha|^2|00\rangle\langle 00| + \alpha\beta^*\sqrt{1-R}\,|00\rangle\langle 10| - \mathrm{i}\alpha\beta^*\sqrt{R}\,|00\rangle\langle 01| \\ &\quad + \alpha^*\beta\sqrt{1-R}\,|10\rangle\langle 00| + |\beta|^2(1-R)|10\rangle\langle 10| \\ &\quad - \mathrm{i}|\beta|^2\sqrt{R(1-R)}\,|10\rangle\langle 01| + \mathrm{i}\alpha^*\beta\sqrt{R}\,|01\rangle\langle 00| \\ &\quad + \mathrm{i}|\beta|^2\sqrt{R(1-R)}\,|01\rangle\langle 10| + |\beta|^2R|01\rangle\langle 01|\,.\end{aligned}$$

The density matrix of the state in channel C is calculated by taking a partial trace over the D states:

$$\begin{aligned}\rho_{\text{out,C}} &= \mathrm{Tr}^{(\text{D})}\rho_{\text{out,CD}} = |\alpha|^2|0\rangle\langle 0| + \alpha\beta^*\sqrt{1-R}\,|0\rangle\langle 1| \\ &\quad + \alpha^*\beta\sqrt{1-R}\,|1\rangle\langle 0| + |\beta|^2R|0\rangle\langle 0| + |\beta|^2(1-R)|1\rangle\langle 1|\,.\end{aligned}$$

Explicitly,

$$\rho_{\text{out,C}} = \begin{pmatrix} |\alpha|^2 + |\beta|^2R, & \alpha^*\beta\sqrt{1-R} \\ \alpha\beta^*\sqrt{1-R}, & |\beta|^2(1-R)\end{pmatrix}.$$

The trace is

$$\mathrm{Tr}\,\rho^2_{\text{out,C}} = 1 - 2|\beta|^4R(1-R)\,.$$

That this is not an entirely mixed state (except in the case $|\beta|^4 = 1$, $R = 0.5$) means that the device can maintain some degree of quantum coherence and therefore satisfies the requirements for a quantum memristor.

The hysteresis dependence in the case under consideration is obtained if the input signal is chosen as $\langle n_{\text{in}}(t)\rangle = |\beta(t)|^2$. The output state is then given by

$$\big\langle n_{\text{out}}(t)\big\rangle = \big(1 - R(t)\big)\big\langle n_{\text{in}}(t)\big\rangle\,.$$

The role of the state parameter, the variable s in (5), is played by the reflection coefficient $R(t)$. Its dependence on time can be specified arbitrarily, to some extent; in [42], this dependence was chosen as

$$R(t) = \big\langle n_{\text{in}}(t)\big\rangle - 0.5\,.$$

Hence,

$$R(t) - R(t-T) = \frac{1}{T}\int_{t-T}^{t}\big(\big\langle n_{\text{in}}(t)\big\rangle - 0.5\big)\,\mathrm{d}t\,, \tag{8}$$

where T is the period over which integration is done at each step of the variation of $R(t)$. The flux of single photons entering channel A changes in time in accordance with the law

$$\big\langle n_{\text{in}}(t)\big\rangle = \big|\beta(t)\big|^2 = \sin^2\frac{\pi t}{T_{\text{osc}}}$$

with the characteristic oscillation period T_{osc}. The dynamics of the device operation is determined by the ratio T/T_{osc}.

The authors of [42] not only described the operation of the system theoretically but also implemented it experimentally. The experimental setup is shown in Fig. 8. A collinear source emits pairs of identical photons at a wavelength of 1550 nm. The source is implemented on a 30-mm PPKTP crystal. The crystal is pumped by a continuous-gain diode laser (Toptica TA Pro 780, USA) with a pump power of about 80 mW. The crystal is inserted into a Sagnac interferometer, which generates photons. One of the photons (idler) is sent directly

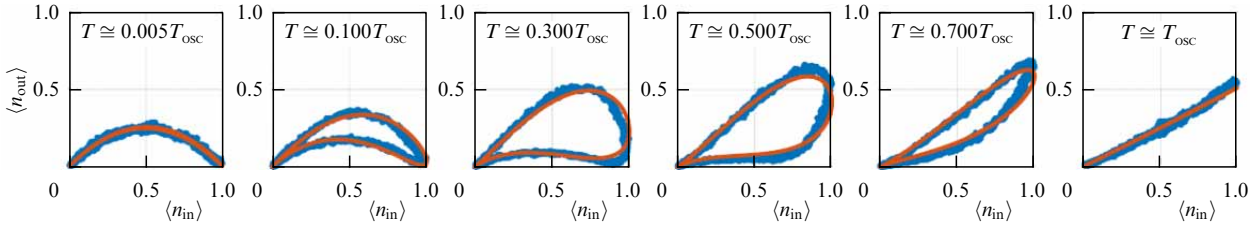

Figure 9. Experimental (blue lines) and theoretical (red lines) dependences of $\langle n_{out} \rangle$ on $\langle n_{in} \rangle$ for different frequency regimes [42].

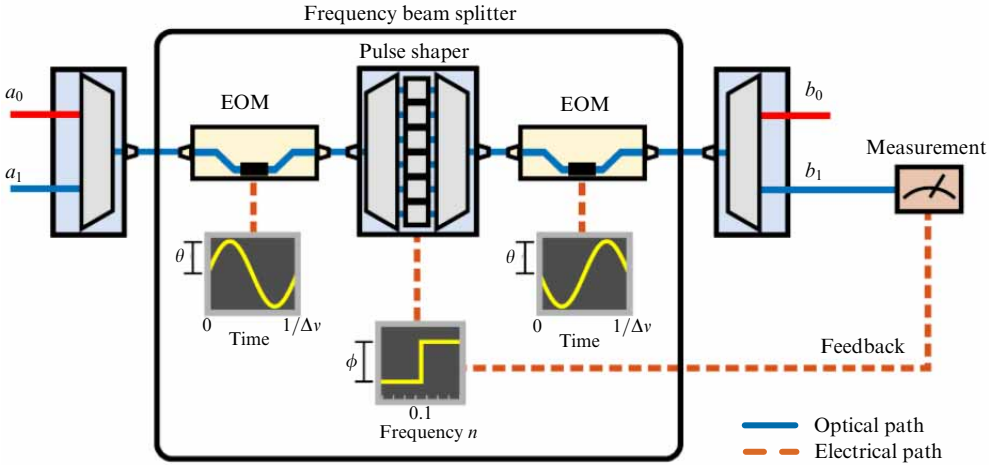

Figure 10. Experimental setup demonstrating a memristor based on a frequency beam splitter [40]. EOM is an electro-optical phase modulator.

to the detectors, and the other (signal) is transmitted to a built-in photonic processor via a single-mode fiber, which is glued directly to its surface. In the photonic processor, the photon goes through a state preparation stage and then enters the quantum memristor. At the output, the processor is connected to single-mode fibers connected to detectors. Superconducting nanowire single-photon detectors (Photonspot Inc., USA) have an average detection efficiency above 95%. A total of three detectors are used: one for the idler photon, one for the feedback signal, and one for the output signal. After the detectors, a logical block analyzes the signals. Each coincidence of the idler and feedback signals triggers the generation of a rectangular voltage pulse in the feedback channel. Similarly, each coincidence of the idler and the output signals triggers a voltage pulse in the output channel. With a pump power of about 80 mW in the source, the maximum coincidence rate in each channel is approximately 3×10^4 samples per second. Both channels are then low-pass filtered with RC filters ($RC = 100$ ms). This gives rise to averaging of the pulse trains and produces a continuous voltage signal proportional to the pulse frequency, which is in turn proportional to the number of photons. Thus, the measurement of the output voltage of the RC filters is a measurement of the expected photon number value. At this instant, the output signal is sent to the oscilloscope for final data recording, while the feedback signal is sent to a microcontroller, which calculates $\langle n_{in} \rangle$ and uses it to update the value of $R(t)$.

The experimental and theoretical dependences in terms of the variables $\langle n_{out} \rangle$ and $\langle n_{in} \rangle$ are shown in Fig. 9.

We note that the setup presented above (see Fig. 7) allows encoding information in the so-called dual-rail regime, when encoding occurs along spatial modes. For example, the $|0\rangle$ state can correspond to a photon in channel A, and the $|1\rangle$ state, to a photon in channel B.

In the studies discussed above, a quantum memristor was constructed from a beam splitter with tunable reflectivity, which could be modified depending on the measurement results in one of the channels. The authors of [40] showed that a similar implementation is possible using frequency-entangled optical fields and a frequency mixer, which, working similarly to a beam splitter, creates superpositions of states. They considered a memristor based on a frequency beam splitter, which is a Hadamard element acting on the frequency degrees of freedom of the input data. To coordinate operations between frequency ranges, they used an electro-optical phase modulator (EOM) and a pulse shaper with a Fourier transform. By cascading EOMs and pulse shapers in an alternating sequence, any frequency-bin unitary can in principle be realized with favorable resource scaling. Figure 10 shows a possible experimental setup for a frequency-bin memristor. The input spectral modes a_0 and a_1 are combined into a single fiber, where they are temporally phase modulated with an amplitude θ and cyclic frequency Δv. In the pulse shaper, a phase shift φ is applied to the modes $n \geqslant 1$ (including those outside the two-dimensional space). A second EOM, driven at the same amplitude as the first, but exactly out of phase, concludes the frequency beam splitter. The output signal b_1 is then extracted and measured, and the results are used to update the phase shift φ of the pulse shaper.

In the output signal detection and feedback circuit implemented here, the phase φ changes depending on the measurement result at the output of the beam splitter coupled to the environment. The other output operates as a response signal of the memristor. The number of photons is measured at the output coupled to the environment, after which the phase φ is changed depending on the average value of the obtained data. In each individual experiment, occurring at a time t_k with a fixed phase $\varphi(t_k)$, the average number of output

photons is obtained and is then used to change the value of φ from $\varphi(t_k)$ to $\varphi(t_{k+1})$.

The photonic platform was further developed in [43], where polaritons — bound states of photons and phonons — were used to obtain the memristive effect. In such devices, the time evolution of the system depends on the ratio of the internal relaxation time of the system to the time of change of its parameters; at some values of this ratio, bistability occurs. The behavior of a polariton-based quantum memristor is controlled by the time dependence of the atomic modulation, providing a hysteresis response of the number of quasiparticles. This mechanism is based on interresonator exchange of polaritons and atomic modulation. The memory effects depend on the initialization of the system (plasticity) and the time scale of the effect.

3. Quantum memristors based on trapped ions

The use of ultracold trapped ions for the implementation of a quantum memristor appears to be very promising due to the presence of a sufficiently large number of ionic levels with different lifetimes and transitions with different 'oscillator strengths,' as well as the possibility of using bound states of ions. The concept of a quantum memristor based on ultracold ions was first proposed and developed in the work of researches from the Lebedev Physical Institute [44, 45].

In the case of an ultracold ion captured in a trap, three levels can be selected: the ground state $|g\rangle$, an excited long-lived state $|e\rangle$, and an excited short-lived state $|a\rangle$. Using various techniques (laser or microwave resonant excitation, or Raman excitation), Rabi oscillations between the $|g\rangle$ and $|e\rangle$ levels can be initiated, which means that, under the action of such a perturbation, periodic transitions from the $|g\rangle$ to the $|e\rangle$ level and back occur. The wave function is then given by the superposition

$$|\Psi_{\text{in}}\rangle = \alpha|g\rangle + \beta|e\rangle\,,$$

where $|\alpha|^2 + |\beta|^2 = 1$. The probability of excitation of the $|e\rangle$ level changes with time t and is given by

$$|\beta|^2 = \sin^2\left(\frac{\Omega t}{2}\right),$$

where Ω is the Rabi frequency for the $|g\rangle \leftrightarrow |e\rangle$ transitions.

Also, by resonantly affecting the ion with another electromagnetic field, a transition from the $|e\rangle$ level to a certain $|a\rangle$ level can be initiated, such that the transition from $|g\rangle$ to $|a\rangle$ does not occur. The transition probability can be controlled by choosing the duration τ of the laser pulse and/or its amplitude. By selecting the values of these parameters, the $|e\rangle \to |a\rangle$ transition probability

$$|\gamma|^2 = \sin^2\left(\frac{\tilde{\Omega} t}{2}\right)$$

(where $\tilde{\Omega}$ is the Rabi frequency for the $|e\rangle \leftrightarrow |a\rangle$ transitions) can be varied in the range from 0 to 1. The wave function of the ion after initiating the $|e\rangle \to |a\rangle$ transition is

$$|\Psi_{\text{out}}\rangle = \alpha|g\rangle + \beta\sqrt{1-|\gamma|^2}\,|e\rangle + \beta\gamma|a\rangle\,.$$

The excitation of the $|a\rangle$ level is recorded using luminescence.

To obtain a hysteresis dependence, we choose the input signal x to be the probability of the ion being in the state $|e\rangle$ before the laser pulse that initiates the $|e\rangle \to |a\rangle$ transition:

$$x = \left|\langle e|\Psi_{\text{in}}\rangle\right|^2 = |\beta|^2\,.$$

The output signal y is the probability of the ion being in the $|e\rangle$ state after the laser pulse that initiates the $|e\rangle \to |a\rangle$ transition:

$$y = \left|\langle e|\Psi_{\text{out}}\rangle\right|^2 = |\beta|^2\left(1-|\gamma|^2\right).$$

The dependence of the output signal on the input signal is then given by

$$y = \left(1-|\gamma|^2\right)x\,. \tag{9}$$

As we have already noted, $|\gamma|^2$ can be changed with time, and therefore this probability plays the role of the state parameter s: $s = |\gamma|^2$. The law by which the state parameter changes over time can be chosen quite arbitrarily, for example, in the form

$$\dot{s} = \frac{1}{T}(x-c)\,, \tag{10}$$

where c is a constant. Equations (9) and (10) are analogous to Eqns (4) and (5) and hence define the memristive behavior of the system with respect to the variables x and y. Integrating (10) over a certain period T, we have

$$s(T) = s(0) + \frac{1}{T}\int_0^T (x-c)\,\mathrm{d}t\,. \tag{11}$$

The procedure for the implementation of a quantum memristor is as follows. At the initial time instant, a certain probability $s(0)$ is fixed and the parameters of the laser radiation initiating the transition $|e\rangle \to |a\rangle$ are set so as to ensure this probability. A period T is selected during which the transitions $|e\rangle \to |a\rangle$ are excited and the population of the $|a\rangle$ level is recorded. The probability of finding the ion in the state $|a\rangle$ is then given by $\langle a\rangle = |\langle a|\Psi_{\text{out}}\rangle|^2 = s(0)x$. Hence, by determining the value of $\langle a\rangle$ experimentally, we can calculate the value of the input signal x on the first period T. Letting x_1 denote this value, we can use formula (9) to obtain the corresponding output signal y_1, and by substituting x_1 in formula (11), we find the new value of the state parameter $s(T)$. For this value of $s(T)$, x_2 and y_2 are calculated in the same way as x_1 and y_1 were calculated, and then $s(2T)$ is found. The procedure is then iterated.

In [44], to study the influence of some laser pulse parameters on the memristive characteristics of the proposed object, the population dynamics of the levels of a three-level system under the influence of a sequence of resonant laser pulses was simulated. For this, a system of equations for the population amplitudes a of the selected levels of an atom interacting with two resonant laser fields was used,

$$\dot{a}_{|g\rangle} = \mathrm{i}\Omega^* \exp\left[-\left(\frac{t-t_{01}}{\tau_1}\right)^2\right] a_{|e\rangle}\,,$$

$$\dot{a}_{|e\rangle} = \mathrm{i}\Omega \exp\left[-\left(\frac{t-t_{01}}{\tau_1}\right)^2\right] a_{|g\rangle} + \mathrm{i}\tilde{\Omega} \exp\left[-\left(\frac{t-t_{02}}{\tau_2}\right)^2\right] a_{|a\rangle}\,,$$

$$\dot{a}_{|a\rangle} = \mathrm{i}\tilde{\Omega}^* \exp\left[-\left(\frac{t-t_{02}}{\tau_2}\right)^2\right] a_{|e\rangle}\,,$$

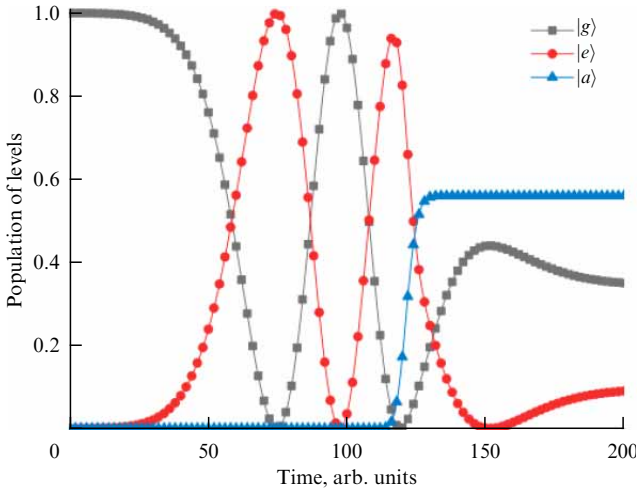

Figure 11. Dynamics of population of $|g\rangle$, $|e\rangle$, and $|a\rangle$ levels calculated for parameter values $\Omega = 0.0755$, $\tilde{\Omega} = 0.09$, $\tau_1 = 50$, $\tau_2 = 0.5$, and $t_{02} - t_{01} = 20$ [44].

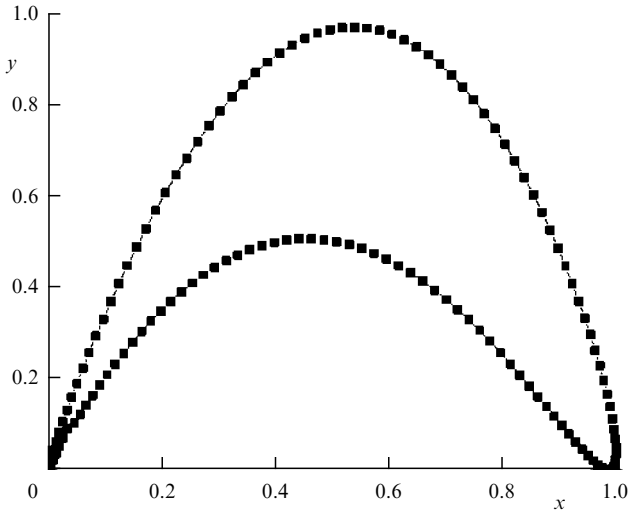

Figure 12. Hysteresis loop in x, y variables [44].

where $t_{02} - t_{01}$ is the time delay between pulses and $\tau_{1,2}$ are the durations of laser pulses. The calculations were performed for the values of Rabi frequencies, durations, and time delays expressed in relative dimensionless units.

Figure 11 shows the dynamics of the population amplitudes of the levels calculated for the parameters $\Omega = 0.0755$, $\tilde{\Omega} = 0.09$, $\tau_1 = 50$, $\tau_2 = 0.5$, and $t_{02} - t_{01} = 20$. It is evident that, under the action of the first pulse, Rabi oscillations are observed for the populations of the $|g\rangle$ and $|e\rangle$ levels. Under the action of the pulse of the second resonant field, the $|a\rangle$ level is excited. For these field parameter values, y and x were calculated and a hysteresis dependence was thus obtained (Fig. 12).

Another possibility of creating the above-described three-level scheme in the $^{171}Yb^+$ ion was analyzed in [45]. It was noted that, first and foremost, the experimental implementation of a quantum memristor on ions requires deep cooling of the ion in a Paul trap. To manipulate a single ion, one can use three-dimensional traps, which are somewhat simpler to manufacture than linear ones and which ensure good optical access to the ion capture region. Ion cooling can be achieved by standard methods, for example, by Doppler or sympathetic laser cooling. The excitation of the $|a\rangle$ state can be registered by the well-known method of quantum jumps (electron shelving). To ensure signal accumulation and reliable registration of the $|a\rangle$ state population, the $|a\rangle$ state lifetime should be much shorter than that of the $|e\rangle$ state. Usually, when implementing the quantum jump method with a wide dipole transition whose line width is tens of MHz, the registration time is about several milliseconds. Therefore, the lifetime of the $|e\rangle$ level should be much longer.

When implementing a quantum memristor on a trapped ultracold $^{171}Yb^+$ ion, there are several options for the set of levels $|g\rangle$, $|e\rangle$, and $|a\rangle$ to be chosen. In the first option, the hyperfine sublevels $^2S_{1/2}$ $(F = 0)$ and $^2S_{1/2}$ $(F = 1)$ of the ground state can serve as respective $|g\rangle$ and $|e\rangle$ levels. The energy difference between these states is 12.6 GHz in a zero applied magnetic field. The only decay mode of the state $^2S_{1/2}$ $(F = 1)$ is a magnetodipole transition to $^2S_{1/2}$ $(F = 0)$. The $|a\rangle$ state can be the shorter-lived state $^2D_{3/2}$ $(F = 2)$, which decays into $^2S_{1/2}$ in about 50 ms. In Fig. 13, such a set of levels and the corresponding transitions are shown in blue.

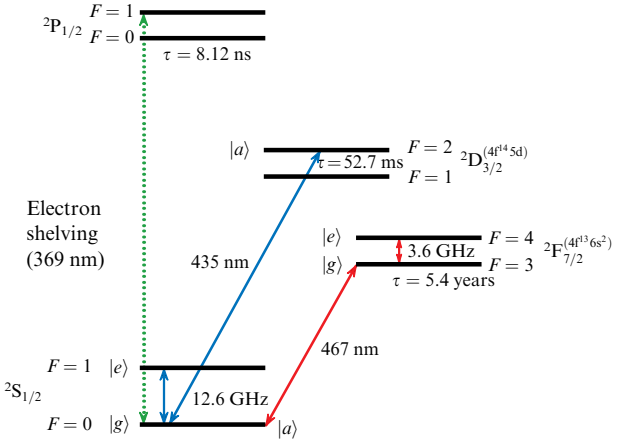

Figure 13. Partial diagram of electron levels of $^{171}Yb^+$ ion (not to scale). Electric dipole transition $^2S_{1/2} \rightarrow {}^2P_{1/2}$ (E1) at a wavelength of 369 nm is used for Doppler cooling and registration of population of ground state of the ion by quantum jump method. Transition between $^2S_{1/2}$ $(F = 0)$ $(|g\rangle)$ and $^2D_{3/2}$ $(F = 2)$ $(|a\rangle)$ levels and transition between $^2S_{1/2}$ $(F = 0)$ and $^2S_{1/2}$ $(F = 1)$ $(|e\rangle)$ hyperfine-structure sublevels of ground state can be used to implement the first single-ion quantum memristor (levels and transitions are shown in blue). Transition between hyperfine structure sublevels $^2F_{7/2}$ $(F = 3)$ $(|g\rangle)$ and $^2F_{7/2}$ $(F = 4)$ $(|e\rangle)$ and between levels $^2F_{7/2}$ $(F = 3)$ and $^2S_{1/2}$ $(F = 0)$ $(|a\rangle)$ can be used to implement the second quantum memristor on a single ion (levels and transitions are shown in red) [45].

In the second option for defining the levels, the hyperfine sublevels of the $^2F_{7/2}$ level can be chosen as $|g\rangle$ and $|e\rangle$. The energy difference between them is 3.6 GHz. The $|g\rangle$ level can be initially populated, for example, by a π-pulse from the ground state. To connect $|g\rangle$ and $|e\rangle$ via a magnetic dipole transition, radio frequency pulses at 3.6 GHz can be used. The only decay channel of the state $^2F_{7/2}$ $(F = 3)$ is the octupole transition to the ground state $^2S_{1/2}$ $(F = 0)$. The $^2S_{1/2}$ ground state can in turn be chosen as the $|a\rangle$ state. Its population can be easily detected using the quantum jump method. A special feature of the proposed scheme is that the $|a\rangle$ level (the ground state of the ion) has a lower energy than $|g\rangle$ does. At the same time, the long lifetime of the $|g\rangle$ level (which significantly exceeds the experiment time) allows one to hope for the successful implementation of this method for defining the levels of a quantum memristor. In Fig. 13, the set of levels and

transitions corresponding to the second option for defining the quantum memristor are shown in red.

Importantly, the presence of two patterns of levels in one ion, with significantly different excitation resonant frequencies, allows proposing a scheme of coupled quantum memristors on a single ion, where the successive action of resonant fields can be used to send the state from memristor to memristor. In addition, the two proposed patterns involve one common level $^2S_{1/2}$ ($F = 0$), which allows such systems to be trained. Two layers of memristors can thus be implemented on a single ion.

It is also noted in [44] that the use of the coupling between ions due to their Coulomb interaction can lead to the creation of coupled quantum memristors on different ions. Obtaining entangled states between ions can allow the use of quantum gates to optimize the operation of a chain of quantum memristors.

4. Quantum memristors on superconducting circuits

Superconducting circuits naturally include memristor elements in Josephson junctions, which were used in the design of a classical superconducting memristor proposed relatively recently [41]. This asymmetrically conducting superconducting quantum interference device (CA-SQUID) could provide hysteretic behavior, but did not include quantum features. In [33], a design of a superconducting quantum memristor was proposed using quasiparticle tunneling for memristive quantum information processing.

The proposed device has the design of a radio frequency SQUID (rf SQUID), shown in Fig. 14. It is a superconducting circuit with an inductance L that contains a built-in small circuit with negligible inductance (DC SQUID), playing the role of a Josephson junction with an externally controlled flux through it. The DC SQUID junctions are made of different materials, and they therefore share the same critical current, but have different conductivities. Hence, the effective critical current in the DC SQUID can be completely suppressed by changing the magnetic flux by $\Phi_0/2$, where Φ_0 is the magnetic flux quantum. Also, passing a magnetic flux Φ_d through the rf SQUID leads to the phase shift

$$\varphi_d = \frac{2\pi\Phi_d}{\Phi_0}\,.$$

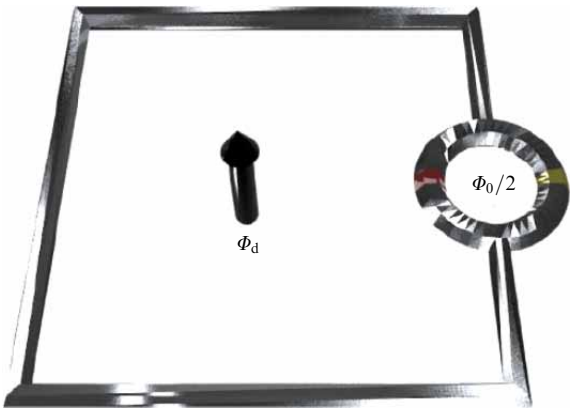

Figure 14. Schematic representation of a superconducting quantum memristor (green and red stripes show transitions with different conductivities) [33].

The Hamiltonian of the system is given by

$$H_s = E_c n^2 + \frac{E_L}{2}\,(\varphi - \varphi_d)^2\,,$$

where n and φ are the Cooper pair number operator and the phase difference (phase shift) operator, E_c is the capacitive energy, and E_L is the inductive energy. The dynamics of the system is confined between the two lower levels of the Hamiltonian H_s. The authors apply an ensemble interpretation of the input and output data of the system, while the mean superconducting phase difference stores information about the past dynamics. Projective nondestructive measurements described in [46] are also used. As a result, the authors show that hysteresis is observed in this device if the mean voltage on the tunneling element is taken as the input parameter and the quasiparticle current is taken as the output parameter.

In [34], a quantum memristor-driven LC circuit was discussed as a quantum memristor paradigm, and the compatibility between memory effects and quantum properties such as coherent superpositions was considered. Continuous measurements were used to preserve coherence [47, 48]. The authors demonstrate a protocol for correctly constructing the evolution equation for superconducting circuits connected to quantum memristors. The model proposed in that paper is conceptual and is not limited to electrical circuits; it can also be studied on other quantum platforms. The paper demonstrates the non-Markovian nature of the dynamics of quantum memristors. The memory effects measured as the hysteresis loop area are shown to be maximized in the classical limit.

Importantly, the superconducting and ionic platforms show remarkable potential for computing the features of open system physics [49].

5. Quantum memristors versus classical memristors

There is currently no clear answer to the question of whether quantum memristors can provide any advantages over classical memristors in neuromorphic computing. Intuitively, it seems that quantum memristors can have greater potential due to quantum superposition and the possibility of using quantum algorithms. However, this problem still needs to be studied in greater detail. We only note a numerical assessment of the efficiency of a quantum reservoir [50, 51] based on quantum memristors given in [42] (Fig. 15). Quantum states of three photons, which can occupy nine different optical modes, are fed to the reservoir input. Next, a matrix of beam splitters with randomly assigned reflectivities is set in place, which mixes information between all modes; after that, the information is sent to the inputs of the memristors. After the memristors, the information is mixed again by a beam splitter array and fed to a photonic detector array, which feeds a small linear readout network with 1,600 adjustable parameters. This quantum reservoir was trained to recognize images from a subset of the MNIST41 handwritten digit database representing the digits 0, 3, and 8; only the readout network was trained. Each image was coarse-grained to 18×12 pixels. The input consisted of one column of pixels at a time, encoded by a simple amplitude scheme. At each step, the quantum memristors were adjusted in accordance with a discrete-time version of Eqn (8). After

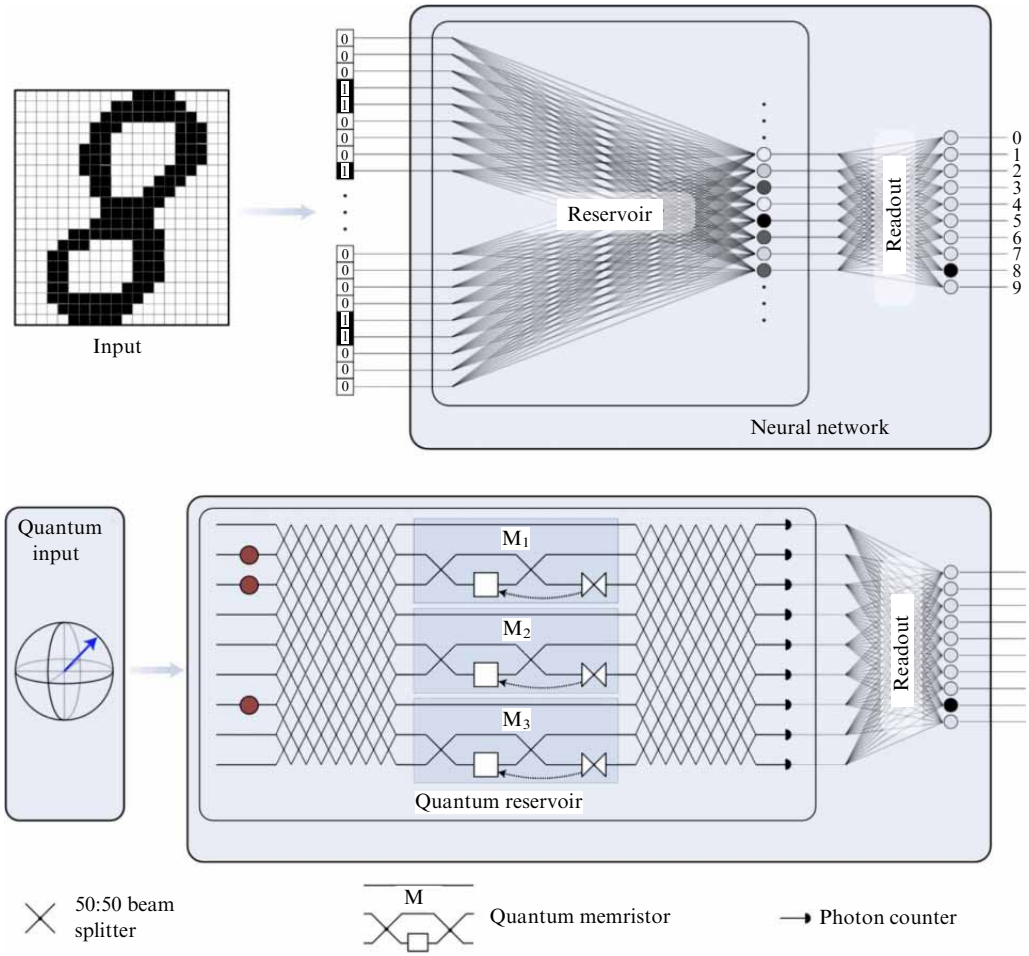

Figure 15. Schematic diagram of quantum reservoir computing [42]. Input information is encoded in a nonlinear multidimensional space, and output data is interpreted by a simple linear readout network. Only the readout network is trained, which requires minimal resources.

training on 1000 different images for 15 cycles, a classification accuracy of 95% was achieved on a test set of 1000 images, not used previously and uniformly distributed over the selected digits.

To have an idea of the quantum advantage of quantum memristors, we performed the same image recognition using only classical information at the input. This was achieved by encoding the input information with classical coherent light instead of single photons, with all other conditions kept the same. As a result, the accuracy of recognizing three digits dropped to about 71%, indicating superior performance in the quantum case. When the quantum memristors were turned off, the accuracy dropped to the level of random guessing. Moreover, in [52, 53], where classical memristors were used for similar reservoirs, accuracies of 91–92% were achieved using 88 memristors or 500,000 adjustable parameters and much larger training sets (14,000 and 60,000).

Of course, these facts do not prove the quantum superiority of the quantum memristor, but they are indicative of a significant potential for its use in neuromorphic computing.

6. Conclusions

According to the data presented, a quantum memristor must include the following components: a tunable dissipative element, weak measurements, and classical feedback. These components can be implemented on different platforms. At present, research into the creation of quantum memristors is only starting. Basically, conceptual ideas are currently available, most of which have not yet found practical implementation. But even a theoretical analysis does not incorporate all possible platforms. In particular, the creation of a quantum memristor on neutral atoms, semiconductors, and other systems is of interest. In addition, the issues of creating coupled quantum memristors using entangled states and quantum algorithms are yet to be studied. Even more difficulties are encountered in the practical construction of quantum memristors, because their necessary components are extremely complex from the standpoint of experimental implementation. We also note that the classical memristor is close in its properties to a synapse, which provides contact between neurons in the brain. At the same time, many scientists, in particular, Penrose [54, 55], who is a Nobel laureate, tend to believe that the work of the brain is determined by the laws of quantum physics. If this is so, then the quantum memristor and computing systems based on it can provide an accurate simulation of the operation of the brain. Moreover, the design and fabrication of quantum memristors, regarded as the main elements in biosimilar learning schemes, entirely belong to nature-based technologies. Research on quantum memristors is an emerging field with great prospects and a number of unresolved issues, which guarantees its rapid development.

Acknowledgments. The study was supported by Russian Science Foundation grant 24-12-00415, https://rscf.ru/project/24-12-00415/.

References

1. Chua L *IEEE Trans. Circuit Theory* **18** 507 (1971)
2. Strukov D B et al. *Nature* **453** 80 (2008)
3. Demin V A, Erokhin V V *Int. J. Unconv. Comput.* **12** 433 (2016)
4. Abraham I *Sci. Rep.* **8** 10972 (2018)
5. Borghetti J et al. *Nature* **464** 873 (2010)
6. Linares-Barranco B, Serrano-Gotarredona T "Memristance can explain spike-time-dependent-plasticity in neural synapses" *Nat. Prec.* (2009) https://doi.org/10.1038/npre.2009.3010.1
7. Alibart F et al. *Adv. Funct. Mater.* **20** 330 (2010)
8. Ielmini D *Semicond. Sci. Technol.* **31** 063002 (2016)
9. Sun K, Chen J, Yan X *Adv. Funct. Mater.* **31** 2006773 (2021)
10. Tominov R et al. *Adv. Electron. Mater.* **8** 2200215 (2022)
11. Tominov R V et al. *Nanoindustriya* (15) 509 (2022)
12. Rylkov V V et al. *J. Exp. Theor. Phys.* **126** 353 (2018); *Zh. Eksp. Teor. Fiz.* **153** 424 (2018)
13. Emelyanov A V et al. *Microelectron. Eng.* **215** 110988 (2019)
14. Yuan L et al. *Adv. Electron. Mater.* **7** 2100432 (2021)
15. van de Burgt Y et al. *Nat. Electron.* **1** 386 (2018)
16. Mu B et al. *J. Mater. Chem. C* **8** 12714 (2020)
17. Park H-L, Lee T-W *Org. Electron.* **98** 106301 (2021)
18. Lapkin D A et al. *Appl. Phys. Lett.* **112** 043302 (2018)
19. Minnekhanov A A et al. *Sci. Rep.* **9** 10800 (2019)
20. Di Ventra M, Pershin Yu V, Chua L O *Proc. IEEE* **97** 1371 (2009)
21. Di Ventra M, Pershin Yu V, Chua L O *Proc. IEEE* **97** 1717 (2009)
22. Jo S H et al. *Nano Lett.* **10** 1297 (2010)
23. Pershin Yu V, Di Ventra M *Neural Networks* **23** 881 (2010)
24. Pershin Yu V, Di Ventra M *Phys. Rev. E* **84** 046703 (2011)
25. Yu S et al. *IEEE Trans. Electron Devices* **58** 2729 (2011)
26. Pershin Yu V, Di Ventra M *Proc. IEEE* **100** 2071 (2012)
27. Thomas A *J. Phys. D* **46** 093001 (2013)
28. Moon J et al. *Nat. Electron.* **2** 480 (2019)
29. Yao P et al. *Nature* **577** 641 (2020)
30. Chua L O, Kang S M *Proc. IEEE* **64** 209 (1976)
31. Caravelli F, Carbajal J P *Technologies* **6** (4) 118 (2018)
32. Sanz M, Lamata L, Solano E *APL Photon.* **3** 080801 (2018)
33. Salmilehto J et al. *Sci. Rep.* **7** 42044 (2017)
34. Pfeiffer P et al. *Sci. Rep.* **6** 29507 (2016)
35. Qiu X et al. *Commun. Mater.* **5** 70 (2024)
36. Aksenov M A et al. *Phys. Rev. A* **107** 052612 (2023)
37. Vishnyakova G A et al. *Phys. Usp.* **59** 168 (2016); *Usp. Fiz. Nauk* **186** 176 (2016)
38. Khabarova K Yu, Kalganova E S, Kolachevsky N N *Phys. Usp.* **61** 203 (2018); *Usp. Fiz. Nauk* **188** 221 (2018)
39. Khabarova K Yu, Zalivako I V, Kolachevsky N N *Phys. Usp.* **65** 1217 (2022); *Usp. Fiz. Nauk* **192** 1305 (2022)
40. Gonzalez-Raya T et al. *Materials* **13** 864 (2020)
41. Kim M S et al. *Phys. Rev. A* **65** 032323 (2002)
42. Spagnolo M et al. *Nat. Photon.* **16** 318 (2022)
43. Norambuena A et al. *Phys. Rev. Appl.* **17** 024056 (2022)
44. Stremoukhov S et al. *Entropy* **25** 1134 (2023)
45. Stremoukhov S Yu et al. *JETP Lett.* **119** 352 (2024); *Pis'ma Zh. Eksp. Teor. Fiz.* **119** 343 (2024)
46. Vool U et al. *Phys. Rev. Lett.* **113** 247001 (2014)
47. Wiseman H M, Milburn G J *Quantum Measurement and Control* (Cambridge, UK: Cambridge Univ. Press, 2010)
48. Jacobs K, Steck D A *Contemp. Phys.* **47** 279 (2006)
49. Kazmina A S et al. *Phys. Rev. A* **109** 032619 (2024)
50. Jaeger H "The 'echo state' approach to analysing and training recurrent neural networks — with an Erratum note," GMD Report No. 148 (Bonn: German National Research Institute for Computer Science, 2001)
51. Maass W, Natschläger T, Markram H *Neural Comput.* **14** 2531 (2002)
52. Du C et al. *Nat. Commun.* **8** 2204 (2017)
53. Jalalvand A, Van Wallendael G, Van de Walle R, in *Proc. of the 7th Intern. Conf. on Computational Intelligence, Communication Systems and Networks, CICSYN 2015, Riga, Latvia, 03–05 June 2015* (Piscataway, NJ: IEEE, 2015) p. 146–151, https://doi.org/10.1109/CICSyN.2015.35
54. Penrose R *The Emperor's New Mind: Concerning Computers, Minds, and the Laws of Physics* (Oxford: Oxford Univ. Press, 1989)
55. Penrose R *Shadows of the Mind: A Search for the Missing Science of Consciousness* (Oxford: Oxford Univ. Press, 1994)